

Article

Electronic Structure Calculations of Rare-Earth-Doped Magnesium Oxide Based on Density Functional Theory

Yanfeng Zhao, Alastair N. Cormack * and Yiquan Wu

Kazuo Inamori School of Engineering, New York State College of Ceramics, Alfred University, Alfred, NY 14802, USA; yz8@alfred.edu (Y.Z.); wuy@alfred.edu (Y.W.)

* Correspondence: cormack@alfred.edu

Abstract: In this paper, the electronic structures of rare earth (Nd, Er)-doped MgO were investigated using density functional theory (DFT), with Hubbard on-site corrections (U_{eff}) applied to rare earth elements. Li was considered a co-dopant. Defect complexes were involved, instead of a single dopant atom, in the supercell. The splitting and distribution of the 4f ground states of Nd and Er dopants in the band gap changed by co-doping Li. The calculation results provide insights into the influences of Li on the optical properties of rare-earth-doped MgO.

Keywords: optical materials; density functional theory; electronic structure; rare earth dopant; magnesium oxide

1. Introduction

During the recent decade, rare-earth-doped crystalline oxides with cubic crystal structures and relatively high thermal conductivity have gained enormous research interest [1–4]. They have a promising potential to provide improved high power laser performance, competing with yttrium aluminium garnet (YAG). Refractory oxide magnesium oxide (MgO) doped with Nd or Er is one of them, under consideration as a solid-state laser gain medium. MgO has a rock-salt structure under ambient conditions [5–7]. Rock-salt MgO possesses a relatively compact crystal structure, with a space volume occupation ratio of 74% [8]. Both Mg and O sit in an octahedral coordination environment.

Neodymium (Nd) and erbium (Er) have been of much interest as optically active dopants in solid-state laser materials. Their long wavelength emissions from 4f manifolds in the near and mid-infrared range have great potential applications in health, military, communication, and many other industries [9–11]. According to the electronic structures of rare earth elements, Nd and Er can provide multiple infrared emissions, especially when being doped into host materials. This potential tunability is essential, especially when consideration must be taken concerning the optical properties of transmission media or the compatibility between the emissions and receiving detectors. For free rare earth elements, the electronic transitions are between the manifolds $^{2S+1}L_J$ ($J = |L - S|, |L - S + 1|, \dots, |L + S - 1|, |L + S|$) from the spectral terms ^{2S+1}L due to spin-orbital coupling. The ground state manifolds of free ionic (3+) Nd ($4f^3$) and Er ($4f^{11}$) are $^4I_{9/2}$ and $^4I_{15/2}$, respectively. The characteristic optical emissions of Nd that are useful for laser applications include electronic transitions from the $^4F_{3/2}$ manifold to the lower manifolds of $^4I_{9/2}$ (900 nm), $^4I_{11/2}$ (1060 nm), $^4I_{13/2}$ (1400 nm), and $^4I_{15/2}$ (1800 nm) [1,12]. Popular emissions of Er are electronic transitions from $^4I_{13/2}$ to $^4I_{15/2}$ (1550 nm) and from $^4I_{11/2}$ to $^4I_{13/2}$ (2700–3000 nm) [13,14]. Each of these manifolds is $2J + 1$ degenerate. For rare earth dopants in the crystal field of the host material, manifolds experience further splitting, and the degeneracies are partially or totally removed, giving Stark levels. The transition terminals become the Stark levels. The extent of the removal of degeneracies is determined by the point symmetry around the dopant site. Moreover, the degree of splitting, or the spread of Stark levels, is determined by the crystal field strength. Though electric dipole



Citation: Zhao, Y.; Cormack, A.N.; Wu, Y. Electronic Structure Calculations of Rare-Earth-Doped Magnesium Oxide Based on Density Functional Theory. *Crystals* **2024**, *14*, 435. <https://doi.org/10.3390/cryst14050435>

Academic Editor: Thomas M. Klapötke

Received: 28 March 2024

Revised: 26 April 2024

Accepted: 1 May 2024

Published: 2 May 2024



Copyright: © 2024 by the authors. Licensee MDPI, Basel, Switzerland. This article is an open access article distributed under the terms and conditions of the Creative Commons Attribution (CC BY) license (<https://creativecommons.org/licenses/by/4.0/>).

transition between 4f manifolds is forbidden according to Laporte's selection rule (parity selection rule), when the crystal field around the dopant lacks a centre of symmetry, the parity selection rule can be mitigated, making intra-configurational transitions happen with greater probabilities [15]. From this perspective, searching for a potential laser host is mainly the search for an optimal crystal field for the rare earth dopants, besides essential mechanical and thermal properties.

Most research on potential laser hosts currently concentrates on experimental synthesis routes and spectroscopic characterisation, although the impact on the optical properties from defects and co-doping has begun to draw considerable attention. Comprehensive synthesis and fabrication routes have been studied on MgO of different forms, such as bulk and nanopowder. Morphological factors can influence the band gap, but the electrically insulating nature is unchanged. For example, MgO nanopowder was synthesised via the solution combustion and hydrothermal methods by Devaraja et al. [16]. Ultraviolet absorption spectra showed two prominent absorption peaks at 240 nm and 290 nm. The main emission peak under 290 nm excitation was found to be centred at 395 nm. Both absorption and emission peaks were identified to be related to F^+ and F centres, which are oxygen vacancies with one and two electrons, respectively. The optical energy gaps were 5.85 eV and 5.50 eV depending on the preparation routes. Bulk transparent MgO ceramics were fabricated via SPS (Spark Plasma Sintering) at a relatively low temperature of 1200 °C by Chen and Wu [17]. Under 265 nm excitation, broad photoemission was observed at 360 nm, which was due to the F^+ centre. The absorption and emission processes occur within the band gap of undoped MgO. The reducing environment of the sintering process contributed to generating the F^+ centres. Nanostructured MgO was investigated concerning the dependence of the band structure on the crystallite size by Kamarulzaman et al. [18] via both experiments and theoretical calculations under the scheme of density functional theory. Experimentally, the band gap was found to narrow from 5.90 eV to 5.84 eV as the crystallite size (the size of crystallite indicates the number of unit cell contained in the crystallite) decreased from 61.66 nm to 1.11 nm. Calculated band gaps increased from 4.684 eV to 4.707 eV with LDA (Local Density Approximation) and 4.772 eV to 4.795 eV with GGA (Generalized Gradient Approximation) as the lattice parameter reduced from 4.2168 Å to 4.2135 Å.

The optical and X-ray absorption spectra of MgO were investigated on a theoretical basis by Begum et al. [19] with DFT and many-body perturbation theory, and DFT calculations with GGA-PBE and hybrid functional HSE gave band gap values around 4.6 eV and 6.6 eV, respectively.

For rare-earth-doped MgO, the positive impact from Li on samples' optical properties has gained much attention. The first successful demonstration of bulk rare earth (Er, Nd)-doped MgO ceramics was reported by Sanamyan et al. [4] with Li introduced as a co-dopant. Three electronic transitions of Nd: MgO for potential laser applications were observed under 808 nm (1.53 eV) excitation. They are ${}^4F_{3/2} \rightarrow {}^4I_{13/2}$, ${}^4F_{3/2} \rightarrow {}^4I_{11/2}$, ${}^4F_{3/2} \rightarrow {}^4I_{9/2}$ with emission peaks at 930–970 nm (~1.31 eV), 1060–1080 nm (~1.16 eV), and 1330–1350 nm (~0.93 eV), respectively. Six emission peaks were observed between 1538 and 1574 nm for Er, Li: MgO due to ${}^4I_{13/2} \rightarrow {}^4I_{15/2}$. The Er-doped sample had better visible transparency than those doped with Nd. Nd, Li: MgO powders were synthesised with a solution combustion method by Oliveira et al. [20]. Radioluminescence and thermal luminescence intensity were greatly enhanced by co-doping Li. The emission peak was around 375 nm (3.31 eV), attributed to electronic relaxations from ${}^4D_{3/2}$ and ${}^2P_{3/2}$ to ${}^4I_{2/9}$. The proposed explanation was that Li provided charge compensation and improved the doping of Nd [21,22]. Er, alkali co-doped (Li, Na, or K) MgO nanopowders were synthesised and characterised by Sivasankari et al. [23]. Despite small changes in crystallite size and lattice constant (based on X-ray diffraction data), the MgO crystal structure was retained after doping, and the alkali elements contributed to better crystallinity.

From the above, pristine MgO has been studied from experimental and theoretical aspects. However, for rare-earth-doped or alkali co-doped MgO, many fewer theoretical

or computational investigations have been made than experimental studies, especially for the mechanism of impact of alkali elements, such as Li. Some explanations were proposed, but few were theoretically validated. The optical properties of crystalline materials depend on many variables such as pores, grain size, and grain boundary. They are fundamentally related to local atomistic scale disorder and induced changes in electronic structures. Presumably, doping rare earth elements into MgO hosts will cause local structural distortions due to ionic size and charge mismatch. From the viewpoint of electronic structure, the changes in the crystal field will induce splitting (decrease in degeneracy) of the 4f manifolds. The positions of the Stark levels determine the wavelength of the photon emitted and the absorptions that may influence the system's transparency at specific wavelengths. The incentive of this work is to understand the role of Li in the optical properties of rare earth (Nd, Er)-doped MgO by electronic structure calculations. Our primary interest is the position and distribution of 4f states in the doped MgO band gap.

2. Computational Details

The calculations based on the density functional theory were carried out with the Vienna Ab initio Simulation Package (VASP 5.4), using plane wave expansions of the wave functions. The projector augmented wave (PAW) pseudopotential was used to treat the valence wave functions. The Generalized Gradient Approximation (GGA-PBE) was used to describe the exchange correlation functional, whose exact form is unknown. As the exchange correlation functional is approximated, the Coulomb interactions are overestimated in the form of Hartree energy, which is the mean field approach to calculate the Coulomb energy of electrons, leading to the delocalisation of electrons. The dopants under current investigations were rare earth elements; they possess characteristic localised electrons in 4f orbitals. In order to improve the electron localisation of 4f orbitals in the calculations, Hubbard on-site correction terms U_{eff} were introduced, based on the method proposed by Dudarev et al. [24]. U_{eff} is the difference between the one-site Coulomb interaction parameter U and the on-site exchange interaction parameter J . J was set to be zero for simplicity.

Crystalline magnesium oxide (MgO) in the cubic phase is the host material investigated in this work. Figure 1 shows the unit cell of the MgO and the coordination octahedron. The O atom and the Mg atom occupy the fractional positions at (0, 0, 0) and (0.5, 0.5, 0.5), respectively. The Mg-O bond length was optimised to be 2.125 Å.

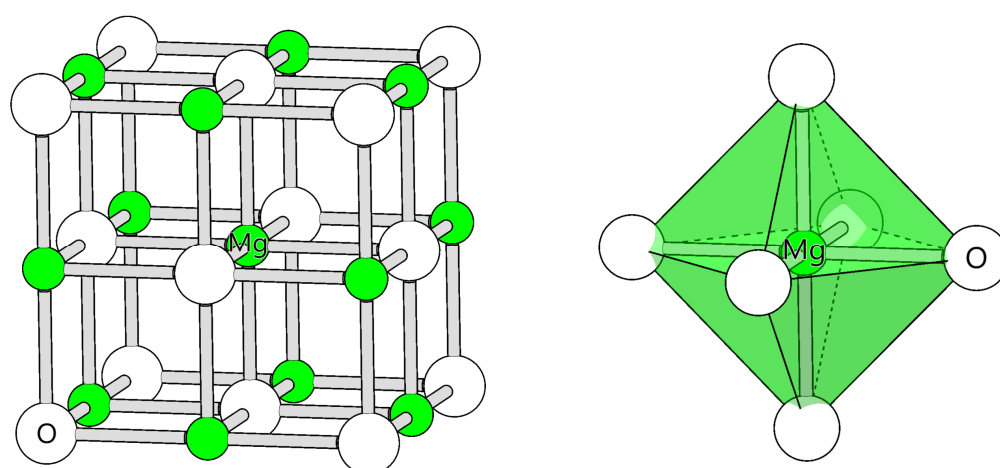


Figure 1. Crystal structure of MgO and coordination of Mg. Green: Mg. White: O.

The dopants considered were neodymium (Nd), erbium (Er), and lithium (Li). The valence electrons of each element involved in the calculations were Mg: $3s^2$; O: $2s^2 2p^4$; Li: $1s^2 2s^1$; Nd: $4f^3 5s^2 5p^6 5d^1 6s^2$; and Er: $4f^{11} 5s^2 5p^6 5d^1 6s^2$. The energy cutoff for the plane wave expansion was chosen to be 600 eV; the results of the convergence tests will be shown

in the next section. An MgO $2 \times 2 \times 2$ supercell was constructed, consisting of 64 atoms. A k point mesh in dimension of $6 \times 6 \times 6$ with the Monkhorst-Pack method [25,26] was used to sample the Brillouin zone. The convergence criteria were $0.3 \text{ eV}/\text{\AA}$ and 1 meV for the ionic and electronic minimisations, respectively. Ionic site optimisation, which is the process of minimising the force on atom, stopped when the force exerted on each atom was less than $0.3 \text{ eV}/\text{\AA}$. The electronic minimisation (after each ionic minimisation) iteration loop stopped when the energy difference between the two successive loops was smaller than 1 meV . A minimum of five steps were performed in the electronic minimisations. The ground state electronic densities were determined by self-consistent static calculations. In doped systems where electroneutral clusters (defect complexes) were contained, the structures of the clusters were the relatively favourable ones found in previous research. The details of the calculations regarding the energetics of defect structures in rare-earth-doped MgO were published elsewhere [27]. A Hubbard on-site correction U_{eff} was applied to the 4f orbitals of the rare earth elements. The optimal U_{eff} for Nd and Er was determined according to the positions of the 4f states in the band gap. The command-line tool developed by Ganose et al. [28] was used to assist in data analysis.

3. Results and Discussion

3.1. Electronic Structures of Pristine Magnesium Oxide

The electronic structure of undoped MgO was investigated first. Considering that the cutoff energy of plane wave expansion and the dimension of the k point mesh are two parameters that largely determine the calculation accuracy, convergence tests were conducted in a MgO unit cell. As shown in Figure 2, cutoff energies ranging from 400 to 700 eV were tested. The lattice constant converged at 4.25 \AA , independent of the cutoff energy.

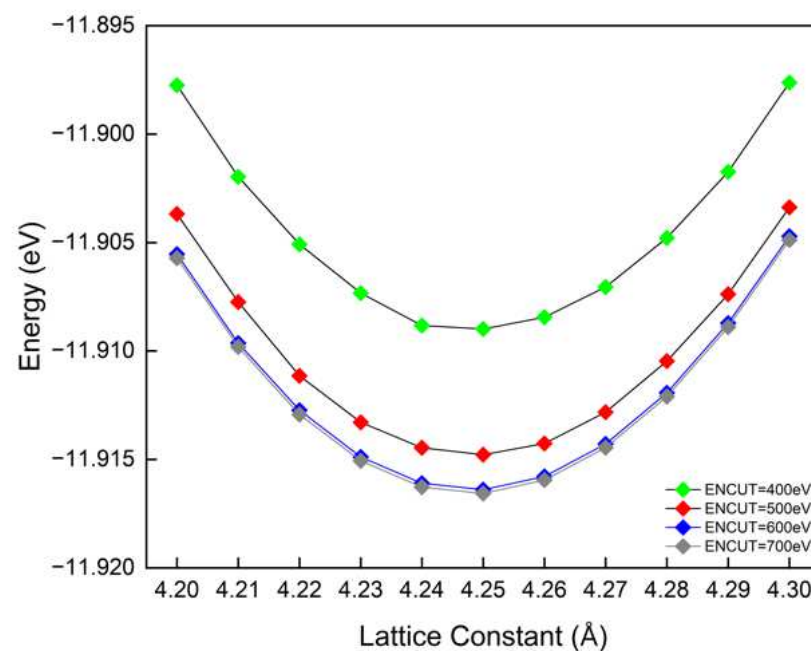


Figure 2. Convergence of plane wave energy cutoff.

The converged lattice constant agrees well with other calculation results [6,19,29,30] but is slightly larger than the experimental value of 4.21 \AA [18]. The overestimation of the lattice constant was also observed in other previous simulations [6,29]. The reason has been suggested to be the underestimation of bonding in the oxide. As these simulations all employed GGA, the reason for an overestimated lattice constant can be further explained: GGA approximates the true exchange-correlation functional, which means the Coulombic

repulsions are still overestimated, including the repulsions between the 2p orbitals of O and 3s orbital of Mg. This results in a greater Mg-O bond length, which further results in a greater lattice constant (Mg-O-Mg). (Another possible reason for the discrepancy between the current calculations and the experimental results could be the differing temperature conditions, with calculations performed at 0 K while experimental measurements are conducted at higher temperatures.) At the converged lattice constant, the energy difference between cutoff energies of 600 eV and 700 eV was on the scale of 1 meV. The dimension of k point mesh was tested from 1 to 10 ($10 \times 10 \times 10$). The energy differences were on the scale of 1 meV when the k point mesh dimension was greater than 6 ($6 \times 6 \times 6$). Therefore, the plane wave cutoff energy of 600 eV and the k point mesh of $6 \times 6 \times 6$ were used, considering a balance between computation accuracy and expense.

Figure 3 shows a combined graph of the band structure (BS) and density of states (DOS) of pristine MgO. BS and DOS provide information about the distribution of electronic states. Whereas the former shows the electronic energy along high symmetry lines in the irreducible Brillouin zone, the latter covers the whole Brillouin zone of the lattice. The high symmetry lines connected with high symmetry points of Γ (0.000, 0.000, 0.000), X (0.500, 0.000, 0.000), U (0.625, 0.250, 0.625), K (0.375, 0.375, 0.750), W (0.500, 0.250, 0.750), and L (0.500, 0.500, 0.500), in fractal coordinates, of the reciprocal lattice were used according to the method proposed by Tanaka and colleagues [31,32].

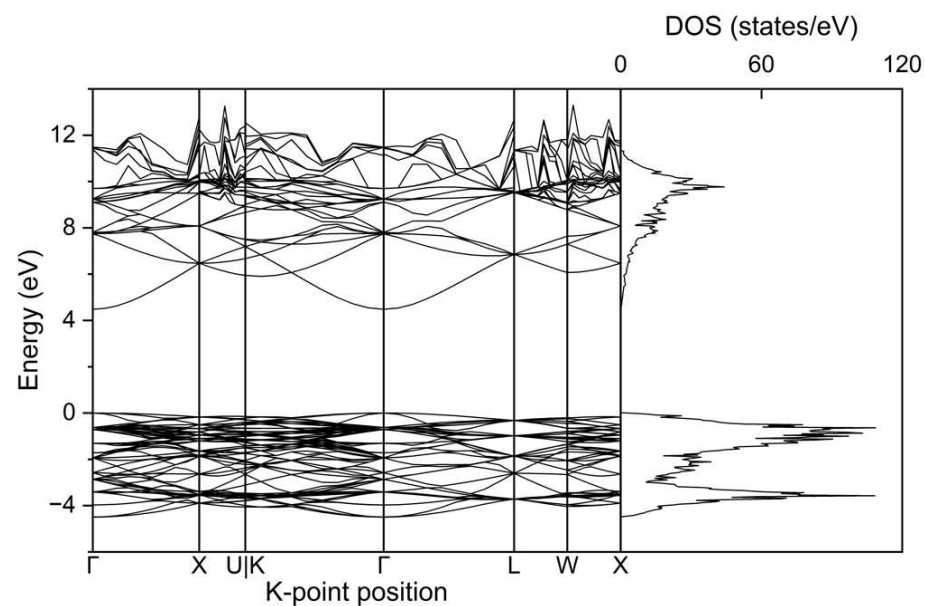


Figure 3. Band structure and total DOS of pristine MgO.

The valence band maximum and conduction band minimum of the band gap were located at the Γ point, indicating that the simulated MgO is a direct band gap material, in agreement with other calculation results. The calculated band gap was 4.58 eV, which is smaller than reported experimental values of 5.5 eV [15], 5.8–5.9 eV [15,18], and 7.2 eV [23]. This difference has been attributed to the framework of density functional theory, where the mutually interacting nature between electrons is approximated by the exchange-correlation functional, which is not exact. The projected contributions from the orbitals of the Mg and O atoms to the band structure of MgO are shown in Figure 4. Both Mg and O atomic orbitals are distributed throughout the valence band and conduction band. The VBM (valence band maximum) is mainly composed of the 2p orbital of the O atom. 2s, 2p of the O atom and 3s of the Mg atom contribute to CBM (conduction band minimum). The O 2p orbital had the most dispersive distribution throughout the band structure of pristine MgO.

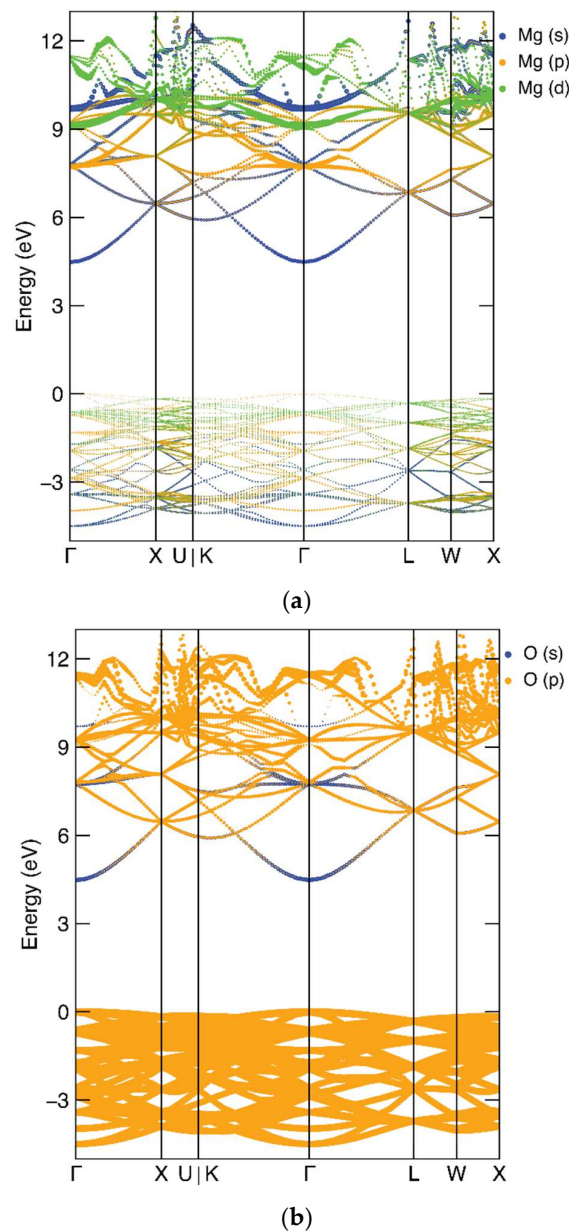
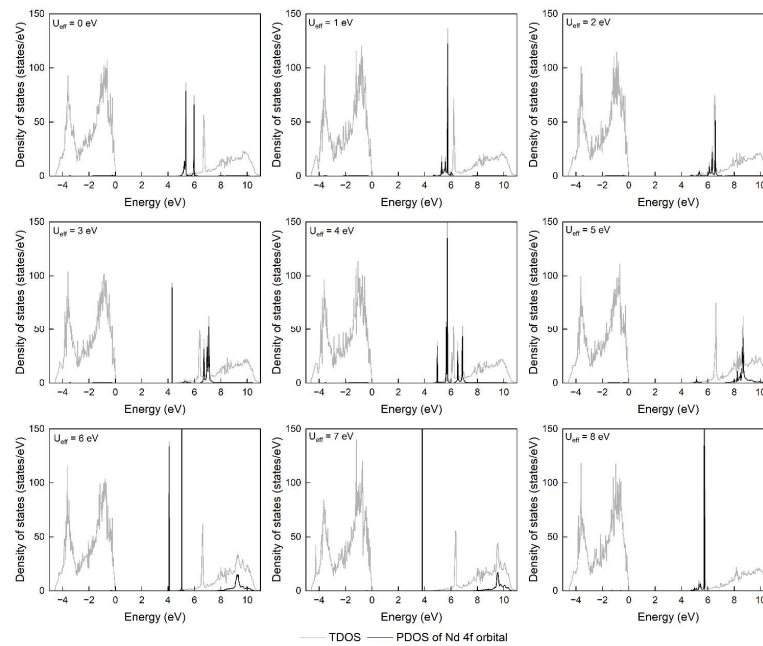


Figure 4. Orbital projected band structure of pristine MgO: (a) s, p, d orbitals of Mg; (b) s, p orbitals of O.

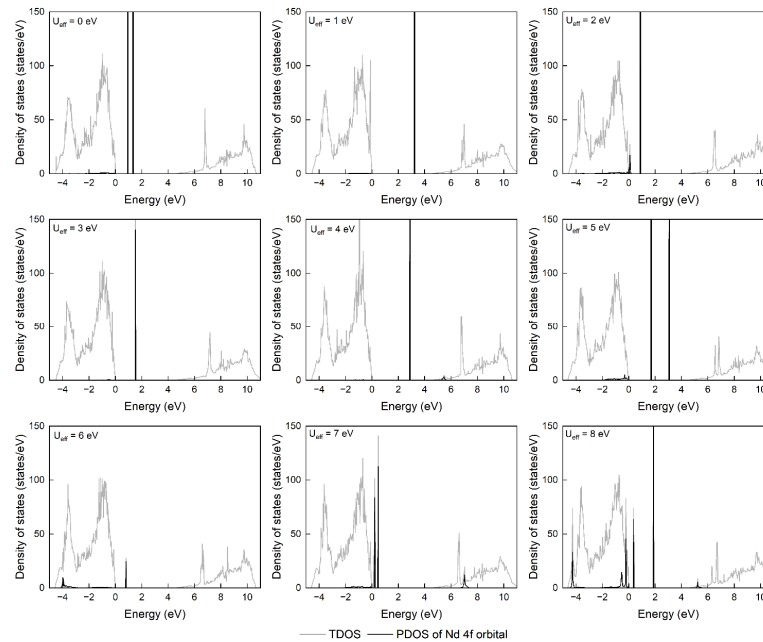
3.2. Hubbard Onsite Parameters of Rare Earth Dopants in Magnesium Oxide

When doping a rare earth ion into a host, it could either replace an occupied site—the substitution site—or occupy an empty site—the interstitial site. Experimentally, it has been proven by X-ray diffraction characterisations [4,21,23] that the structure of rare-earth-doped crystalline MgO remained cubic, indicating that rare earth dopants occupy the substitution sites. In the current simulations, the rare earth elements were placed in substitutional Mg sites. To aid the localisation of the 4f states of the Nd and Er dopants, U_{eff} on-site correction terms were applied. The electronic structures of the single-rare-earth-atom-doped MgO were calculated and compared using different U_{eff} (integer values from 0 to 8 eV). One Mg atom was substituted by one Nd or Er atom in a $2 \times 2 \times 2$ MgO supercell. The aim of these tests was to determine a U_{eff} for each of Nd and Er and use them in the subsequent calculations in the next parts, where the influence of Li will be investigated in systems with defect complexes.

Different U_{eff} values resulted in changes in the following two aspects: (1) the position of the 4f ground states in the band gap and (2) the splitting of the 4f ground state energy. The latter shows how dispersive the energy of the 4f state is, which indicates the localisation status of 4f states. The results are shown in Figure 5a,b, in which the 4f states are highlighted with vertical black lines. When choosing the optimal U_{eff} parameters according to the calculated density of states, the priority was to see whether the applications of U_{eff} positively influence the localisations of 4f states.



(a)



(b)

Figure 5. Density of states of rare-earth-doped MgO, U_{eff} ranges from 0 to 8 eV: (a) Nd: MgO; (b) Er: MgO.

For the Nd dopant, as shown in Figure 5a, when no on-site correction is applied ($U_{\text{eff}} = 0$ eV), two main ground state 4f peaks of similar intensity locate near the CBM, and the energy gap between the two peaks is 0.62 eV. When increasing U_{eff} from 1 to 4 eV, the peak of the highest intensity 4f states for each applied U_{eff} remains near the CBM, but multiple splitting peaks appear. The highest-intensity peak moves towards the top of the conduction band with $U_{\text{eff}} = 5$ eV. As U_{eff} increases to 6 eV and 7 eV, compared to $U_{\text{eff}} = 0$ eV, the energy gap between the splitting 4f peaks becomes larger because of the peak location near the top of the conduction band. When $U_{\text{eff}} = 8$ eV, the 4f ground state spikes near the CBM with small peaks close to its lower energy side. By comparing, $U_{\text{eff}} = 8$ eV gives the most localised 4f ground state in energy. Since no other U_{eff} parameters aid the localisation of 4f of Nd as $U_{\text{eff}} = 8$ eV does, $U_{\text{eff}} = 8$ eV was chosen for the Nd 4f orbitals.

For the Er dopant, as shown in Figure 5b, the 4f ground states distribute mainly between the VBM and the middle of the band gap. $U_{\text{eff}} = 0$ eV gives two 4f ground state peaks of comparable intensities and an energy gap of 0.4 eV, located at 0.9 eV and 1.3 eV above the VBM. The 4f states show good localisations when using $U_{\text{eff}} = 1$ eV, 2 eV, 3 eV, and 4 eV. Though there is a peak 0.1 eV above the VBM for $U_{\text{eff}} = 2$ eV, its intensity is much lower than the main peak, and the 4f energy states mostly localise 0.88 eV above the VBM. Increasing the U_{eff} to larger than 4 eV results in a large splitting of the energy of the 4f states. For example, when $U_{\text{eff}} = 6$ eV, there is a 4f peak at the bottom of the valence band, the other located 0.81 eV above the VBM. When $U_{\text{eff}} = 8$ eV, 4f peaks distribute from the bottom of the valence band to the bottom of the conduction band. To choose a U_{eff} from 1 eV, 2 eV, 3 eV, and 4 eV for Er 4f orbitals, the locations of the 4f states in the band gap were compared with the energy level diagram built by Oliveira et al. [21], where the 4f state of trivalent Er locates 0.4 eV below the VBM. In the current results, the gaps between the main 4f states of Er and the VBM using $U_{\text{eff}} = 1$ eV, 2 eV, 3 eV, and 4 eV are 3.2 eV, 0.9 eV, 1.5 eV, and 2.9 eV, respectively. The 4f state of Er is relatively closer to the VBM when using $U_{\text{eff}} = 2$ eV than using 1 eV, 3 eV, and 4 eV. Thus, $U_{\text{eff}} = 2$ eV was chosen for the Er 4f orbitals.

3.3. Electronic Structures of Rare-Earth-Doped Magnesium Oxide and Roles of Li

The unfilled 4f orbitals of rare earth elements are the inner orbitals. When putting rare earth dopants in a crystalline host, the outer orbitals, the filled 5s and 5p orbitals weaken or screen the perturbation on 4f orbitals from the crystal field. Therefore, the wavelength of the characteristic 4f-4f emission is considered to remain similar in various hosts with similar moderate crystal field strength. But, the energy level in the band gap may change due to the defects in the doped systems. The calculations in this part include electroneutral defect clusters $(2\text{RE}_{\text{Mg}}^{\bullet} + \text{V}_{\text{Mg}}^{//})_{\text{complex}}$ and $(2\text{RE}_{\text{Mg}}^{\bullet} + 2\text{Li}_{\text{Mg}}^{//})_{\text{complex}}$ in $2 \times 2 \times 2$ supercells, where RE = rare earth = Nd or Er. The initial and relaxed structures of the simulated supercells are shown in Figure 6.

As shown in Figure 6, after relaxation, the coordination polyhedra of RE dopants were distorted from the perfect octahedron of Mg of perfect centre-symmetry in pristine MgO. The octahedral coordination remained for substitutional dopants, considering the ionic size and that the rock salt is a compact crystal structure. Changes were more readily observable in the Nd-doped systems than in Er-doped systems. The mismatch in the ionic radii between rare earth and Mg undoubtedly distorts the coordination polyhedron. Quantitatively, the octahedra of two rare earth dopants in the defect complexes were included in the brief statistical analysis of each doped system, as shown in Figure 7.

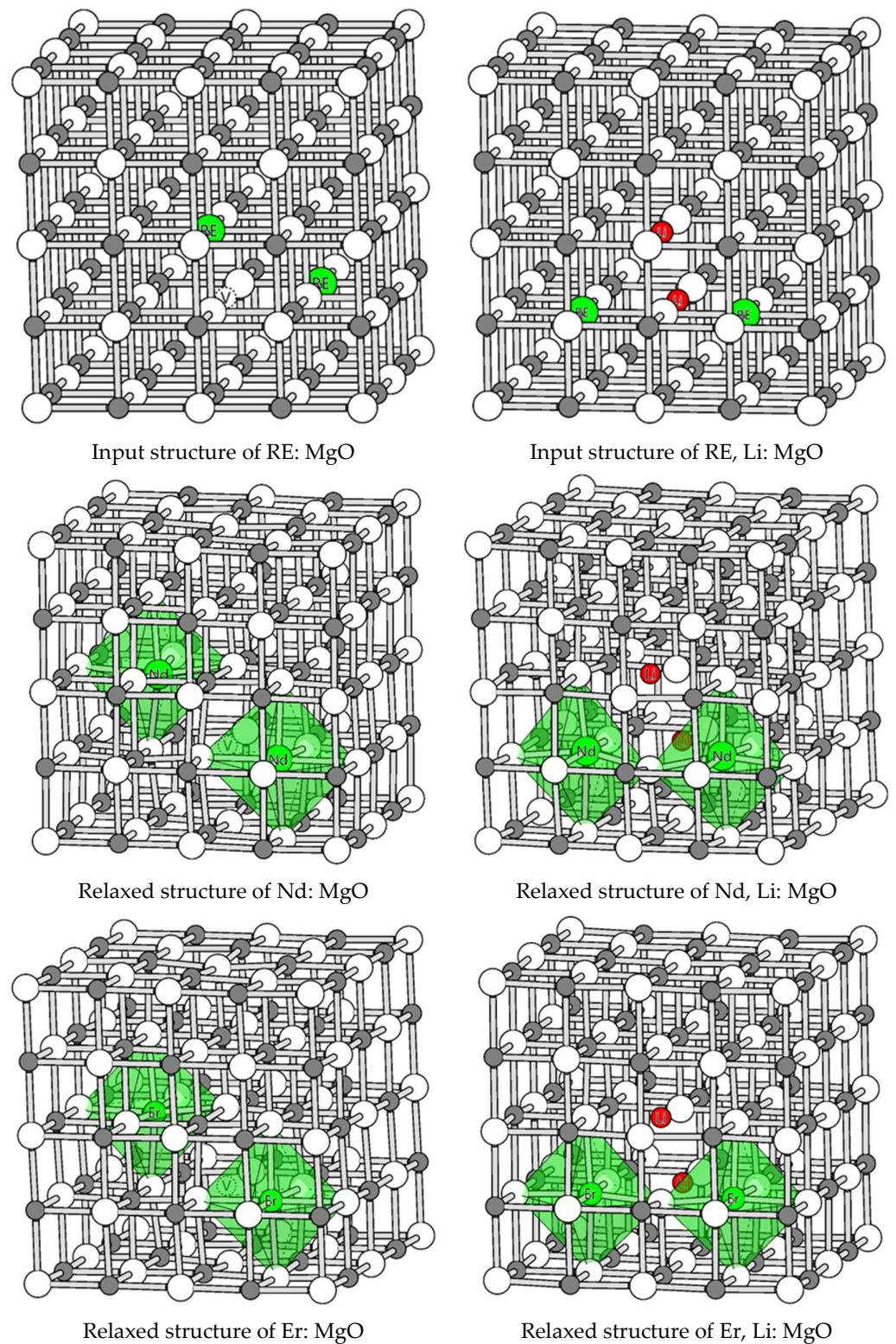


Figure 6. Initial and relaxed supercells of RE: MgO and RE, Li: MgO. RE: Nd or Er. V: Mg vacancy.

The dashed line in the middle indicates the Mg-O bond length in the pristine MgO, which is 2.125 Å. The bond lengths of the rare earth dopant are the interatomic distances between the rare earth dopant and its six nearest oxygen atoms. As the coordinates of each atom in the system are available from the calculations, the inter-atomic distances can be readily obtained. There are six RE-O bonds in each coordination polyhedron. The mean RE-O bond lengths in all four calculated systems were greater than 2.125 Å. This increase

in the bond length is understandable as both Nd and Er possess larger ionic radii than Mg. Under the energy equilibrium condition, oxygen atoms move to a farther distance to relax. As ionic Nd is larger than Er, the mean Nd-O length is larger than the mean Er-O length. Decreases in the mean, maximum, and minimum bond lengths were found in Li co-doped systems. The decrease is more apparent in Nd-doped MgO than in Er-doped MgO.

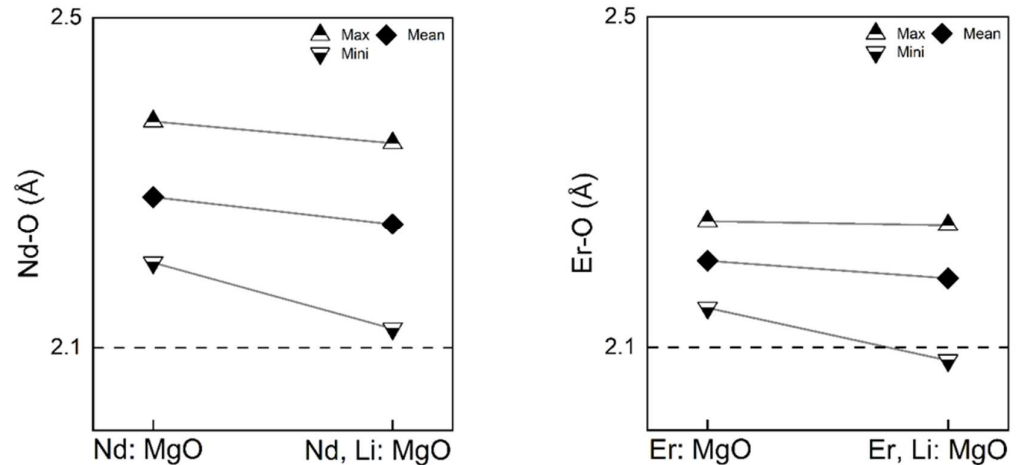


Figure 7. Bond lengths of RE: MgO and RE, Li: MgO (RE = Nd or Er) from DFT calculations.

Comparing the current results in Figure 7 with the results in our previous work [27], as shown in Figure 8, the extent of the relaxations in the bond lengths of the dopant-centred octahedra are consistent, such as the maximum, mean, and minimum bond lengths. The results in Figure 8 were obtained using a classical force-field method—the static lattice method—where the defect relaxations were performed under the Mott–Littleton scheme. The bond lengths considered were also the six nearest oxygen atoms around the rare earth dopant. Both results show that RE, Li: MgO possesses a slightly more contracted octahedra with smaller bond lengths than RE: MgO. Additionally, the distortions of the coordination octahedra of rare earth dopants were quantified using Baur’s Distortion Indices (DI) [33,34], as shown in Table 1. The DI of bond length (TO), bond angle (OTO), and edge length (OO) are expressed as follows:

$$DI(\text{TO}) = \left(\sum_{i=1}^6 |d_i - d_m| \right) / 6 * d_m \quad (1)$$

$$DI(\text{OTO}) = \left(\sum_{i=1}^{12} |\alpha_i - \alpha_m| \right) / 12 * \alpha_m \quad (2)$$

$$DI(\text{OO}) = \left(\sum_{i=1}^{12} |l_i - l_m| \right) / 12 * l_m \quad (3)$$

The DI of the coordination octahedra of the rare earth dopants increased after co-doping Li. However, in the previous simulations based on the classical static lattice method [27], the DI was found to decrease after co-doping Li. This discrepancy results from the different simulation methodologies applied in the two investigations. The defect structures in the static lattice method were relaxed under the Mott–Littleton scheme, and the DFT calculations were based on the periodic boundary condition, where the size of the supercell is of the volume of several unit cells. The size the supercell is limited to the computational resources/power available.

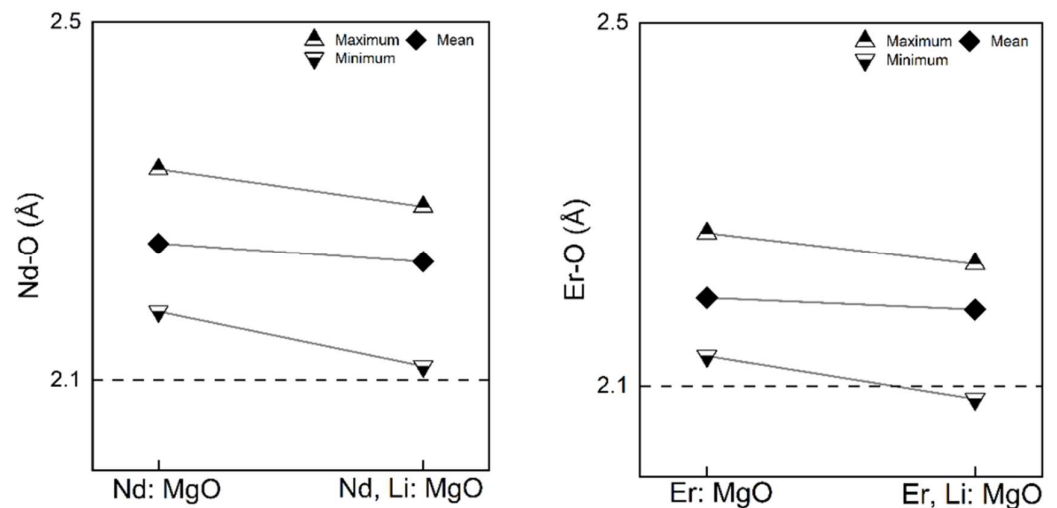


Figure 8. Bond lengths of RE: MgO and RE, Li: MgO (RE = Nd or Er) from static lattice calculations [27].

Table 1. Distortion indices of coordination octahedra of rare earth dopants.

Average DI	Nd: MgO	Nd, Li: MgO
Bond length distortion (TO)	0.0230	0.0290
Bond angle distortion (OTO)	0.0575	0.0660
Edge length distortion (OO)	0.0280	0.0420
Average DI	Er: MgO	Er, Li: MgO
Bond length distortion (TO)	0.0165	0.0175
Bond angle distortion (OTO)	0.0350	0.0310
Edge length distortion (OO)	0.0155	0.0205

The DOS calculation results of defect complexes containing RE: MgO (RE = Nd or Er) with and without Li are shown in Figure 9a,b. For Nd: MgO, by comparing the DOS curves in Figure 5a, which involves no defect cluster, changes can be found mainly in the multiple additional energy levels, especially in the band gap, which are dominated by Nd dopants. The distributions of 4f states were found to be different. The introduction of the complex contributes to a broader spread of 4f ground states, which is due to the interaction between the closely situated dopants [35]. According to Figure 9a, overlapping of 4f and 5d states was observed in the CB (conduction band), and the peak of the highest intensity of Nd 4f states lies at a higher energy than that of 5d states in the CB. With this energy distribution, the parity allowed 4f-5d transitions become more accessible. At the same time, this may depress the forbidden intra-configurational 4f-4f transitions. On the other hand, since 5d states lie in the CB, where electrons are delocalised, 4f-5d transitions would be hard to observe experimentally. In a cluster-free system, 5d states lie right below the CBM. When using the band gap of the experimental value (~7.2 eV) [23], for the systems with defect complexes, the 5d states lie below the CBM with an energy gap smaller than 1 eV. This is smaller than the one in the system with an isolated dopant. This indicates that the probability of electrons being excited from 5d to the conduction band is higher in clustered systems. Two peaks were observed in the band gap, contributed by the 4f states of the two Nd dopants. One lies around 0.1 eV above VBM, and the other lies around 3.2 eV above VBM, giving a width of 3.1 eV. The former peak possesses a higher intensity. The grey area between the peaks is used to indicate this gap.

The distribution of 4f states in the band gap was a critical change when comparing cluster-doped systems with and without Li co-doping. In Nd, Li: MgO, two peaks of the 4f states were located at 0.3 eV and 3.1 eV above VBM with an increased density of states, giving a smaller energy width of 2.8 eV. Some 4f peaks were found at the lower energy side of the 5d states in Nd: MgO, but these peaks disappeared in Nd, Li: MgO. This change may discourage the absorption transition from 4f to 5d ground states, as the energy gap between 5d and the lower energy 4f states vastly increases.

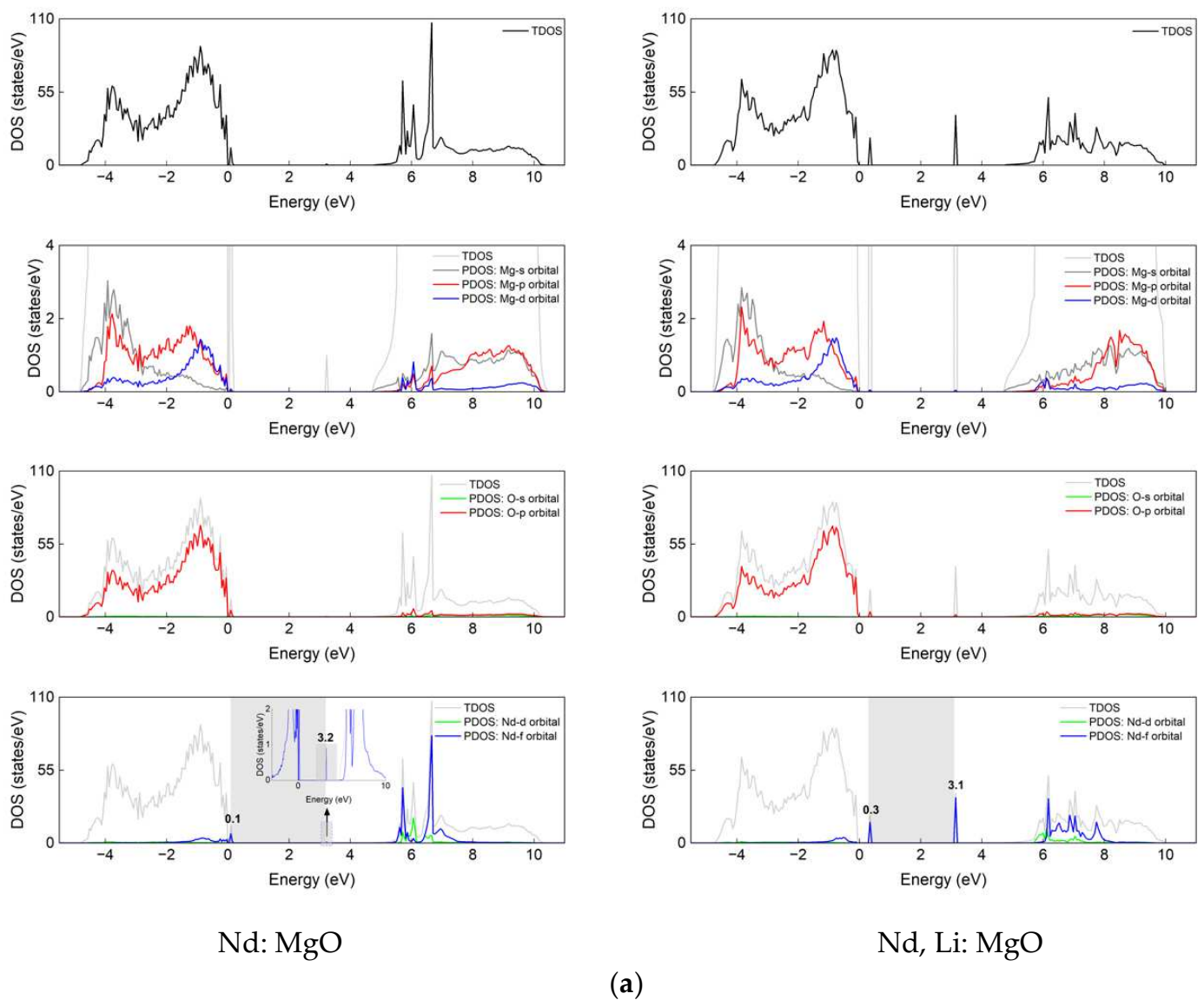


Figure 9. Cont.

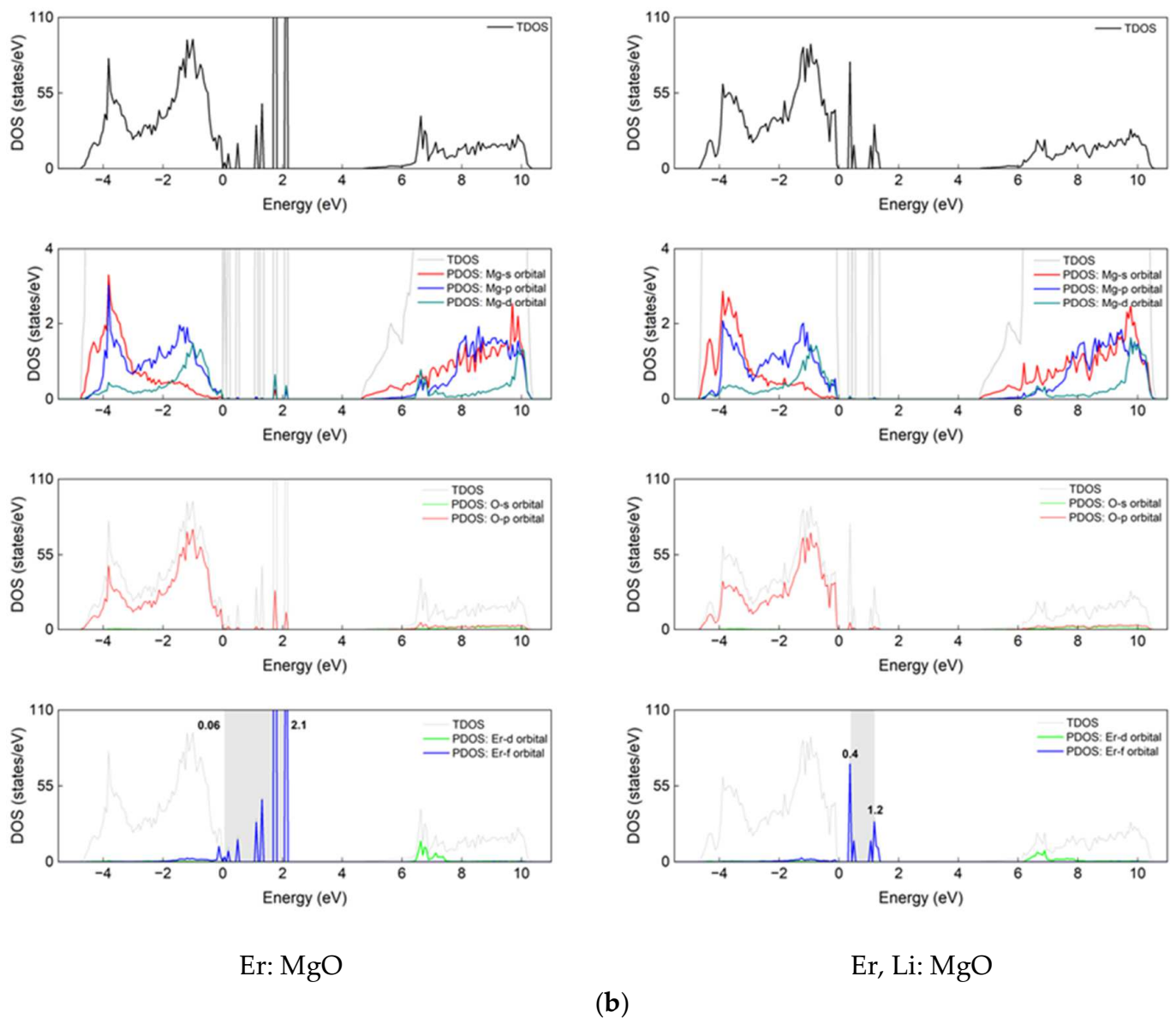


Figure 9. DOS of (a) Nd: MgO and Nd, Li: MgO. (b) Er: MgO and Er, Li: MgO.

In the Er: MgO with defect complexes, as shown in Figure 9b, the distribution of the 4f ground states of Er was found to be relatively more dispersive than in Figure 5b. The energies of the 4f states of Er: MgO and Er, Li: MgO range from 0.06 to 2.1 eV and from 0.4 to 1.2 eV in the band gap, respectively, giving energy widths of 2.04 eV and 0.8 eV. A larger energy width means a more dispersive energy distribution of the 4f states. In Er: MgO, one Er dopant contributes to the peaks of lower energies, and the other Er dopant contributes to the peaks of higher energies in the band gap. In Er, Li: MgO, each Er dopant contributes to all peaks in the band gap. An essential difference between the distributions of the 4f states of Nd and Er is that the 4f states of Er distribute within the band gap. Its 5d states remain in the CB without overlapping with 4f states. In the Nd-doped system, 4f states emerge on both the lower and higher energy sides of the 5d states, indicating that both absorption and emission towards 5d may occur. Nevertheless, in the Er-doped system, only absorbing energy can excite electrons from 4f to 5d states. The probability of 4f-5d transitions in Nd: MgO may be higher than in Er: MgO, regardless of Li. Additionally, after the cooperation of Li, the number of Er 4f levels in the band gap decreased. The intensity of peaks of the lower energy increased, while peak intensities of the higher energy decreased.

Compared to Er: MgO, the distribution of the ground 4f states in the band gap of Er, Li: MgO are more localised. This is favourable to obtain a narrow emission peak and increased emission intensity.

The projected DOS from Li orbitals are shown in Figure 10. Both the s and p orbitals of Li spread through the valence band, the conduction band, and the band gap but with a very low peak intensity. An overlapping with the peaks of 4f states in the band gap was observed.

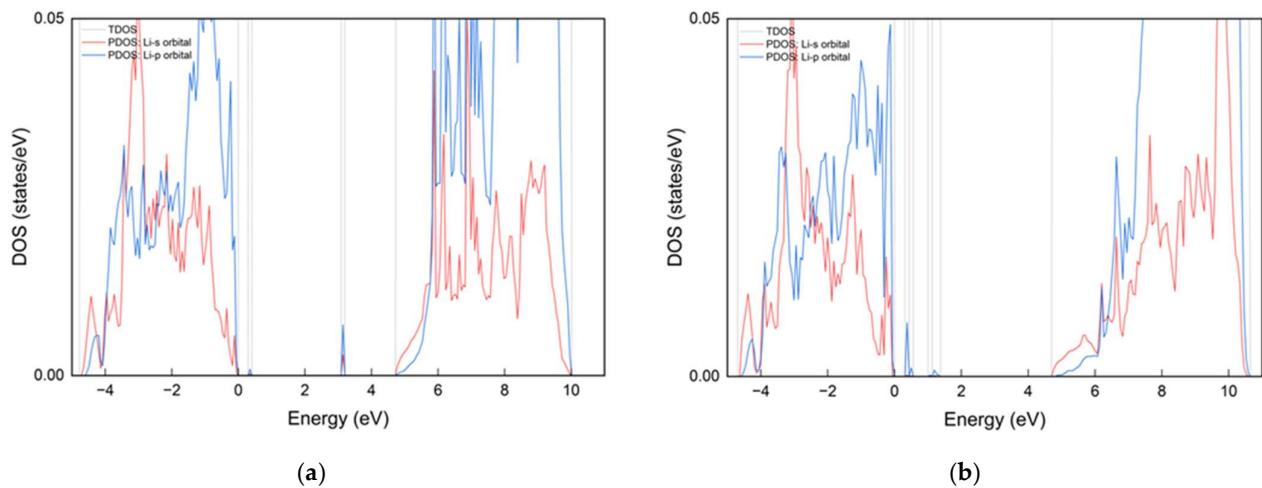


Figure 10. PDOS of co-dopant Li in RE, Li: MgO, RE = Nd or Er: (a) Nd, Li: MgO; (b) Er, Li: MgO.

A simplified illustration of the band structures of calculated systems is shown in Figure 11. The blue lines are 4f levels, and the green lines are 5d levels. Given the physical origin of energy level splitting in a crystal field, the calculated ground 4f energy levels in the band gap of Nd- and Er-doped systems can be interpreted as the Stark levels, which belong to the ground state manifolds of ${}^4I_{9/2}$ and ${}^4I_{15/2}$, respectively. ${}^4I_{9/2}$ and ${}^4I_{15/2}$ possess 10 and 16 $(2J + 1)$ degeneracies in total, respectively. Since Nd^{3+} and Er^{3+} ions possess an odd number of 4f electrons, each Stark level has a minimum of 2-fold degeneracy, independent of the point symmetry of the crystal field [15,36]. The calculated 4f energy levels were not given further notation as the reduction degree of the respective ground state manifolds was not resolved so far. However, the number of calculated main 4f peaks contributed by each dopant were fewer than five for Nd or eight for Er. The results do not conflict with the degeneracy characteristics of $4f^3$ and $4f^{11}$. The VBMs were shifted to zero. The CBM was positioned according to experimental results of the band gap of pristine crystalline MgO [23], which is around 7.2 eV above the VBM. Possible resonant absorptions of photons can be presumed from the energy gaps between the calculated energy levels in the band gap. As for the popular wavelength of Nd and Er, 1060 nm (~ 1.2 eV) is expected to have good transparency in Nd (Li): MgO. Li was not found to induce electronic energy levels for resonant absorption at that wavelength. In Er, Li: MgO, resonant absorptions of 1550 nm (~ 0.8 eV) may happen. However, Er possesses multiple emissions in the range of 1538–1574 nm. Good transparency can be expected as well in this range. As indicated by the black arrows, potential absorptions of wavelength in the visible range in Nd: MgO include 400 nm from the occupied to upper 4f states and 517 nm from the lower to upper 4f states. In Nd, Li: MgO, a possible absorption is 443 nm from the 4f states in the band gap. In Er: MgO, potential absorptions include 729 nm, 653 nm, and 620 nm among the 4f states in the band gap. However, no potential resonant absorptions are expected in the visible range in Er, Li: MgO.

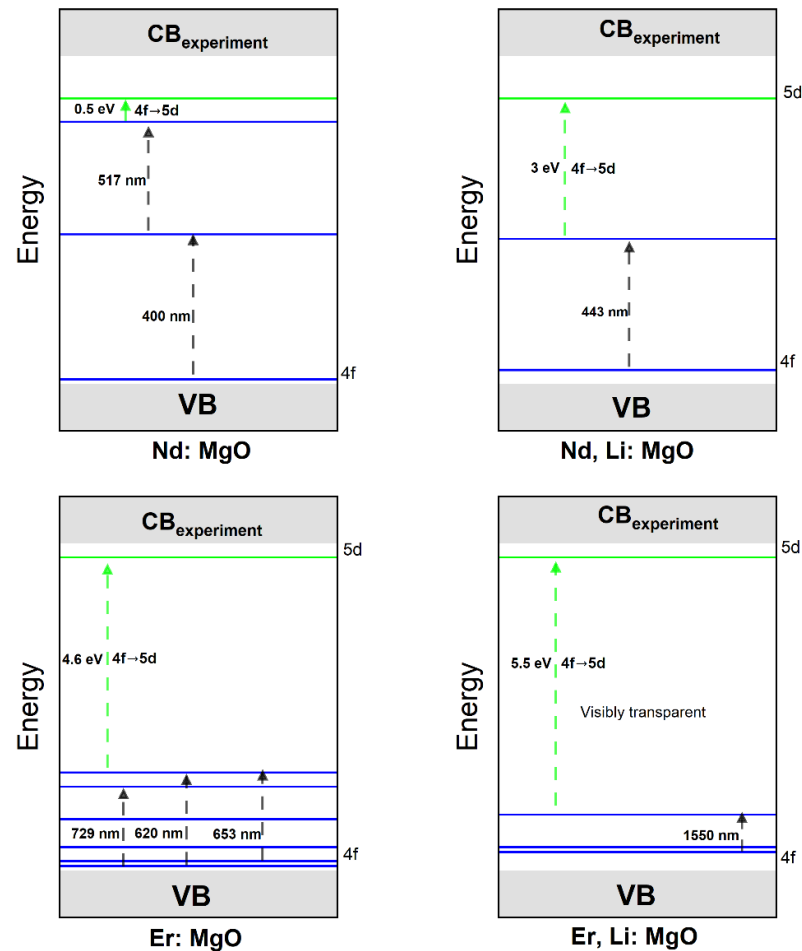


Figure 11. Conceptual band structure of RE, Li: MgO, RE = Nd or Er.

Based on the above, Li co-doping may influence the transparency of Nd- and Er-doped MgO in the visible range. Er, Li: MgO has better visible transparency than Nd, Li: MgO. This may partially explain the experimental results of the relative visible transparency between Er- and Nd-doped MgO co-doped with Li [4]. The starting levels of these potential absorptions are from the low Stark levels. The depopulation of the electrons on these levels may be beneficial for maintaining the population inversion between them and the Stark levels which belong to upper excited manifolds. The equilibrium between this absorption and the stimulated/spontaneous emission will determine the ultimate optical properties.

In all, the changes in the electronic structures by co-doping Li include the following aspects: (1) density of the 4f states (peak intensity) in the band gap, (2) energy gap between the 5d states and the 4f states, and (3) position and splitting of the 4f states in the band gap. For potential laser applications where a reverse population between the excited and the ground 4f states is the basis, if fewer 4f electrons jump upwards to 5d states, more would be available for 4f-4f transitions. These results suggest that Li co-doping may contribute to the laser property of both Nd: MgO and Er: MgO, but the underlying mechanisms are considered to be different. The former two aspects may weigh more for Nd: MgO, and the latter may weigh more for Er: MgO, depending on in which system those changes are relatively more apparent.

4. Conclusions

This paper investigated the electronic structures of pristine and rare-earth-doped MgO under the DFT + U_{eff} (PAW-PBE). First, a lattice constant of 4.25 Å and a band gap of 4.55 eV were derived for undoped MgO, which agreed well with the other calculation results.

Secondly, rare earth (Nd and Er)-doped MgO was investigated. U_{eff} values of 8 eV and 2 eV were used for Nd and Er, respectively, in the calculations involving defect complexes. From the viewpoint of atomic structure, a decrease in mean bond length was found after Li co-doping, indicating slight shrinkage of their octahedral coordination geometries.

According to the calculation results of the density of states, 4f peaks of Nd and Er were found to be more dispersive in the cluster-contained systems compared to isolated single dopant systems. Notably, the dispersion of the calculated splitting of the 4f ground states was larger compared to 0.01–0.1 eV, which is the degree of Stark splitting of 4f manifolds in different crystal fields [37]. This might be due to the interactions between closely located rare earth dopants. The crystal field becomes strong and less symmetrical when dopants are locally concentrated, which causes increased splitting. Validation of this hypothesis would require calculations of crystal field strength. In the current simulations, as the defect clusters were involved in supercells, the interactions between the dopants within the cluster and the adjacent supercells may both be responsible. The supercell approach may limit the extent of relaxation around the defect cluster. One way to resolve their contributions could be to weaken the interaction between supercells by expanding the size of the supercells used in simulations at the expense of increasing computational resources, which was not possible in this work.

Secondly, the electronic structures of Nd- and Er-doped MgO were found to change similarly when incorporating Li. The splitting magnitude of 4f ground states was found to decrease. These changes in the distribution of 4f energy levels can be related to the change in the distortion of the coordination octahedra of rare earth dopants. According to Walsh [15], the splitting of 4f states is influenced by the crystal field in the crystalline host. In systems co-doped with Li (substituting on Mg sites), Li breaks the periodicity of the host crystal field and distorts the coordination octahedra by increasing the Baur Distortion Indices, resulting in a decreased crystal field strength, thus resulting in 4f states with less splitting. This shrinkage in 4f energy levels resulted in an increased energy gap between the 5d level and the 4f level below. With Li co-doping, it is anticipated that an efficient pumping process would favour a more localised set of Stark levels of the Nd and Er ground manifolds. In the pumping process, if the 4f ground states have dispersive distributions, the 4f electrons will be pumped to many different upper excited levels. Electrons in different excited levels may relax in different ways and that may result in difficulty achieving population inversion, which relies on the pumped electrons relaxing to a certain metastable state. The calculated electronic structures also indicate possible absorptions of wavelengths in the visible range of doped systems. Li co-doping may influence the colouration of rare-earth-doped MgO. Er: MgO co-doped with Li possesses the most potential to be visibly transparent. This may partially explain the experimental findings in the difference in the visible transparency among samples doped with Nd and Er [4]. No resonant transitions in visible wavelengths were found between the calculated energy levels within the band gap, assuming that scattering from pores, grain boundaries, and other colouration sources are ideally controlled and play trivial roles. Good transparency at around 1060 nm is promising in Nd (Li)-doped MgO, and absorption at around 1550 nm in Er, Li: MgO may occur. A more in-depth investigation of the properties related to laser processes requires determining the specific Stark levels. Besides the ground state electronic structure of the doped system, the excited levels should be known. Calculations of the 4f excited states, their positions in the band structure, their transition probabilities, and their interatomic energy transfer will be the focus of future investigations. The current results revealed the impact of Li on the crystal structure—the coordination geometry of rare earth dopants and the ground state electronic structures of rare earth (Nd and Er)-doped MgO—providing a theoretical basis for further investigations of mechanisms of Li and encouraging practical tailoring of the optical properties of rare-earth-doped solid-state laser materials.

Author Contributions: Conceptualisation, A.N.C. and Y.W.; Investigation, Y.Z., A.N.C. and Y.W.; Methodology, A.N.C.; Supervision, A.N.C. and Y.W.; Writing—original draft, Y.Z.; Writing—review and editing, A.N.C. and Y.W. All authors have read and agreed to the published version of the manuscript.

Funding: This research received no external funding.

Data Availability Statement: The original contributions presented in the study are included in the article; further inquiries can be directed to the corresponding author.

Acknowledgments: The theoretical calculations were performed using the computing resources at Inamori School of Engineering of New York State College of Ceramics, Alfred University. Y.Z. would like to thank Yiquan Wu and Alastair N. Cormack for formulating the topic and methodology of this work and thank Alfred University for the studentships.

Conflicts of Interest: The authors declare no conflicts of interest.

References

1. Liu, Z.; Ikesue, A.; Li, J. Research progress and prospects of rare-earth doped sesquioxide laser ceramics. *J. Eur. Ceram. Soc.* **2021**, *41*, 3895–3910. [[CrossRef](#)]
2. Wu, X.; Tang, L.; Hardin, C.L.; Dames, C.; Kodera, Y.; Garay, J.E. Thermal conductivity and management in laser gain materials: A nano/microstructural perspective. *J. Appl. Phys.* **2022**, *131*, 020902. [[CrossRef](#)]
3. Kim, W.; Baker, C.; Villalobos, G.; Shaw, L.B.; Sadowski, B.; Frantz, J.; Aggarwal, I.D.; Sanghera, J.S. Ceramic materials for high power solid state lasers. *Proc. SPIE* **2012**, *8235*, 823508.
4. Sanamyan, T.; Cooper, C.; Gilde, G.; Sutorik, A.C.; Dubinskii, M. Fabrication and spectroscopic properties of transparent Nd³⁺:MgO and Er³⁺:MgO ceramics. *Laser Phys. Lett.* **2014**, *11*, 065801. [[CrossRef](#)]
5. Peng, H.; Lany, S. Polymorphic energy ordering of MgO, ZnO, GaN, and MnO within the random phase approximation. *Phys. Rev. B* **2013**, *87*, 174113. [[CrossRef](#)]
6. Schleife, A.; Fuchs, F.; Furthmüller, J.; Bechstedt, F. First-principles studies of ground-and excited-state properties of MgO, ZnO, and CdO polymorphs. *Phys. Rev. B* **2006**, *73*, 245212. [[CrossRef](#)]
7. Ataide, C.A.; Pelá, R.R.; Marques, M.; Teles, L.K.; Furthmüller, J.; Bechstedt, F. Fast and accurate approximate quasiparticle band structure calculations of ZnO, CdO, and MgO polymorphs. *Phys. Rev. B* **2017**, *95*, 045126. [[CrossRef](#)]
8. Smyth, D.M. *The Defect Chemistry of Metal Oxides*; Oxford University Press: New York, NY, USA, 2000.
9. Ahmed, S.A.; Mohsin, M.; Ali, S.M.Z. Survey and technological analysis of laser and its defense applications. *Def. Technol.* **2021**, *17*, 583–592. [[CrossRef](#)]
10. Tzanakakis, E.-G.C.; Skoulas, E.; Pepelassi, E.; Koidis, P.; Tzoutzas, I.G. The use of lasers in dental materials: A review. *Materials* **2021**, *14*, 3370. [[CrossRef](#)]
11. Walsh, B.M.; Lee, H.R.; Barnes, N.P. Mid-infrared lasers for remote sensing applications. *J. Lumin.* **2016**, *169*, 400–405. [[CrossRef](#)]
12. Cai, Y.; Xu, B.; Zhang, Y.; Tian, Q.; Xu, X.; Song, Q.; Li, D.; Xu, J.; Buchvarov, I. High power and energy generation in a Nd: YAG single-crystal fiber laser at 1834 nm. *Photonics Res.* **2019**, *7*, 162–166. [[CrossRef](#)]
13. Nie, H.; Wang, F.; Liu, J.; Yang, K.; Zhang, B.; He, J. Rare-earth ions-doped mid-infrared (2.7–3 μm) bulk lasers: A review. *Chin. Opt. Lett.* **2021**, *19*, 091407. [[CrossRef](#)]
14. Chen, X.; Yao, T.; Huang, L.; An, Y.; Wu, H.; Pan, Z.; Zhou, P. Functional fibers and functional fiber-based components for high-power lasers. *Adv. Fiber Mater.* **2023**, *5*, 59–106. [[CrossRef](#)]
15. Walsh, B.M. Judd-Ofelt theory: Principle and practice. In *Advances in Spectroscopy for Lasers and Sensing*; Springer: Dordrecht, The Netherlands, 2006; pp. 403–433.
16. Devaraja, P.B.; Avadhani, D.N.; Prashantha, S.C.; Nagabhushana, H.; Sharma, S.C.; Nagabhushana, B.M.; Nagaswarupa, H.P. Synthesis, structural and luminescence studies of magnesium oxide nanopowder. *Spectrochim. Acta A Mol. Biomol. Spectrosc.* **2014**, *118*, 847–851. [[CrossRef](#)] [[PubMed](#)]
17. Chen, X.; Wu, Y. Fabrication and Optical Properties of Highly Transparent MgO Ceramics by Spark Plasma Sintering. *Scr. Mater.* **2019**, *162*, 14–17. [[CrossRef](#)]
18. Kamarulzaman, N.; Mustaffa, D.T.; Chayed, N.F.; Badar, N.; Taib, M.F.M.; Ibrahim, A.B.M.A. Comparison of experimental and first-principle results of bandgap narrowing of MgO nanostructures and their dependence on crystal structural parameters. *Appl. Nanosci.* **2018**, *8*, 1621–1628. [[CrossRef](#)]
19. Begum, V.; Gruner, M.E.; Vorwerk, C.; Pentcheva, R. Theoretical description of optical and X-ray absorption spectra of MgO including many-body effects. *Phys. Rev. B* **2020**, *103*, 195128. [[CrossRef](#)]
20. Oliveira, L.C.; Milliken, E.D.; Yukihara, E.G. Development and characterization of MgO: Nd, Li synthesized by solution combustion synthesis for 2D optically stimulated luminescence dosimetry. *J. Lumin.* **2013**, *133*, 211–216. [[CrossRef](#)]
21. Oliveira, L.C.; Yukihara, E.G.; Baffa, O. Lanthanide-doped MgO: A case study on how to design new phosphors for dosimetry with tailored luminescent properties. *J. Lumin.* **2019**, *209*, 21–30. [[CrossRef](#)]

22. Orante-Barrón, V.R.; Oliveira, L.C.; Kelly, J.B.; Milliken, E.D.; Denis, G.; Jacobsohn, L.G.; Puckette, J.; Yukihiro, E.G. Luminescence properties of MgO produced by solution combustion synthesis and doped with lanthanides and Li. *J. Lumin.* **2011**, *131*, 1058–1065. [[CrossRef](#)]
23. Sivasankari, J.; Sellaiyan, S.S.; Sankar, S.; Devi, L.V.; Sivaji, K. Structural and optical characterization of Er-alkali-metals co-doped MgO nanoparticles synthesized by solution combustion route. *Phys. E Low Dimens. Syst. Nanostruct.* **2017**, *85*, 152–159. [[CrossRef](#)]
24. Dudarev, S.L.; Botton, G.A.; Savrasov, S.Y.; Humphreys, C.J.; Sutton, A.P. Electron-energy-loss spectra and the structural stability of nickel oxide: An LSDAU study. *Phys. Rev. B* **1998**, *57*, 1505–1509. [[CrossRef](#)]
25. Lee, J. *Computational Materials Science: An Introduction*, 2nd ed.; CRC Press: Boca Raton, FL, USA, 2016.
26. Monkhorst, H.J.; Pack, J.D. Special points for Brillouin-zone integrations. *Phys. Rev. B* **1976**, *13*, 5188–5192. [[CrossRef](#)]
27. Zhao, Y.; Cormack, A.N.; Wu, Y. Atomistic simulations of defect structures in rare earth doped magnesium oxide. *Crystal* **2024**, *14*, 384. [[CrossRef](#)]
28. Ganose, A.M.; Jackson, A.J.; Scanlon, D.O. sumo: Command-line tools for plotting and analysis of periodic ab initio calculations. *J. Open Source Softw.* **2018**, *3*, 717. [[CrossRef](#)]
29. Gueddim, A.; Bouarissa, N.; Villesuzanne, A. First-principles determination of structural properties of MgO. *Phys. Scr.* **2009**, *80*, 055702. [[CrossRef](#)]
30. Karki, R.B.; Stixrude, J.L.; Clark, S.J.; Arren, M.C.W.; Ackland, I.G.J.; Crainj, J.A. Structure and elasticity of MgO at high pressure. *Am. Miner.* **1997**, *82*, 51–60. [[CrossRef](#)]
31. Hinuma, Y.; Pizzi, G.; Kumagai, Y.; Oba, F.; Tanaka, I. Band structure diagram paths based on crystallography. *Comput. Mater. Sci.* **2017**, *128*, 140–184. [[CrossRef](#)]
32. Togo, A.; Tanaka, I. Spglib: A software library for crystal symmetry search. *arXiv* **2018**, arXiv:1808.01590.
33. Baur, W.H. The geometry of polyhedral distortions. Predictive relationships for the phosphate group. *Acta Cryst. B* **1974**, *30*, 1195–1215. [[CrossRef](#)]
34. Ertl, A.; Hughes, J.M.; Pertlik, F.; Foit, F.F.; Wright, S.E.; Brandstatter, F.; Marler, B. Polyhedron Distortions in Tourmaline. *Can. Miner.* **2002**, *40*, 153–162. [[CrossRef](#)]
35. Canning, A.; Chaudhry, A.; Boutchko, R.; Grønbech-Jensen, N. First-principles study of luminescence in Ce-doped inorganic scintillators. *Phys. Rev. B Condens. Matter Mater. Phys.* **2011**, *83*, 125115. [[CrossRef](#)]
36. Hehlen, M.P.; Brik, M.G.; Krämer, K.W. 50th anniversary of the Judd-Ofelt theory: An experimentalist's view of the formalism and its application. *J. Lumin.* **2013**, *136*, 221–239. [[CrossRef](#)]
37. Brik, M.G.; Ma, C.-G. *Theoretical Spectroscopy of Transition Metal and Rare Earth Ions: From Free State to Crystal Field*; Jenny Stanford Publishing: Singapore, 2019.

Disclaimer/Publisher's Note: The statements, opinions and data contained in all publications are solely those of the individual author(s) and contributor(s) and not of MDPI and/or the editor(s). MDPI and/or the editor(s) disclaim responsibility for any injury to people or property resulting from any ideas, methods, instructions or products referred to in the content.